ORIGINAL RESEARCH ARTICLE

Formation of Peripheral Coarse Grain in Thin-Walled Al–Mg–Si Extrusion Profiles

P. GOIK, A. SCHIFFL, and H.W. HÖPPEL

Investigations on microstructure and texture development during processing of Al–Mg–Si sheet and extrusion profiles focused on describing and modelling the changes in the bulk. However, understanding the evolution of microstructure in the sub-surface region is highly relevant, as this governs material performance under corrosion and bending deformation, which are crucial applications in mobility and transportation. The aim of this study was to correlate the effect of alloy composition and extrusion parameters to the formation of texture and peripheral coarse grain (PCG) layer. For this, five alloys of the AA6xxx class with varying content of dispersoid forming elements were extruded at increasing extrusion speeds into thin-walled hollow profiles. The microstructure at a plane section was investigated by means of EBSD and characterized in terms of distinct texture component distribution. It was shown that with increasing grain boundary mobility, through adapting dispersoid content and extrusion speed, the PCG layer grows into a fine-grained bulk. This growth of the PCG layer is only counter-acted upon, when the grain boundary mobility in the bulk is high enough, so that extensive growth of Cube oriented grains occurs. The PCG layer shows distinct orientations related to ⟨101⟩||TD, so that a possible mechanism for the orientation selection during grain growth is proposed.

https://doi.org/10.1007/s11661-023-07144-3

I. INTRODUCTION

THE application profile on structural safety components in transportation such as automobiles, busses and trains demand for high strength and ductility of the material. This is necessary to absorb maximum crash energy in case of an accident, while retaining lightweight potential for construction. Extrusion profiles of age-hardening Al–Mg–Si alloys fulfill these requirements including a high degree of hot workability due to a low strength at high temperature and a sufficient strength in the final state after age hardening.[1] While the age hardening process affects both strength and ductility,[2,3] the grain microstructure and texture developing during the hot working process primarily influence the ductility and formability of the final material state.[4–6]

Development of grain structure and texture of Al–Mg–Si alloys depend on the alloy chemistry and the initial microstructure after casting and homogenization heat treatment prior to the hot working step. Most of the microstructure and texture evolution of wrought aluminum alloys during working has been performed on sheet alloys of different classes of wrought alloys, such as pure Al,[7,8] Al–Mn,[9–11] Al–Mg[12,13] and Al–Mg–Si.[4,14–16] Although the chemistry of these alloy classes is different, the mechanisms of microstructure and texture formation are related and depend on the following factors:

I. plastic deformation mechanism governed by the matrix' crystal system
II. effects of phases on the plastic deformation mechanism
III. applied strain state and temperature during deformation
IV. driving forces on recrystallization and grain growth

Regarding the first factor, Hirsch and Lücke[7] identified that texture formation is linked to the plastic deformation mechanism of the fcc crystal structure of Al with a medium to high stacking fault energy, depending on the alloy composition and the working temperature, which in turn affect the number of elements in solid solution during forming. Metals with a high stacking fault energy show a small tendency for twinning under

P. GOIK and H. W. HÖPPEL are with the Department of Materials Science & Engineering, Institute I: General Materials Properties, Friedrich-Alexander-Universität Erlangen-Nürnberg, Martensstraße 5, 91058 Erlangen, Germany. Contact e-mail: philip.goik@fau.de A. SCHIFFL is with the Hammerer Aluminium Industries Extrusion GmbH, Lamprechtshausener Straße 69, 5282 Ranshofen, Austria.
Manuscript submitted January 27, 2023; accepted July 13, 2023.
Article published online August 1, 2023

deformation. Cold rolling of such metals leads to the formation of the Copper $\{112\}\langle 111\rangle$ texture component. Introduction of an increasing number of soluble elements in the solid solution reduces the stacking fault energy and shifts the resulting texture after cold rolling to the Brass $\{011\}\langle 211\rangle$ texture component. The formation of these distinct texture components is explained by the Taylor Model,[17] taking into account the lattice rotation that is affected either by slip or twinning deformation. Deformation textures of alloys are then characterized by the spread between those texture components along the β orientation fiber.

The second factor describes the role of particles that are formed prior to the extrusion process, and are not soluble in the solid solution. In Al alloys Fe plays an important role for the formation of such particles. Fe is present as an impurity in technical alloys with a very low solubility in fcc α-Al.[18] Depending on the exact chemical composition and heat treatment during casting and homogenization, this leads to the formation of Al_3Fe, α- and β-AlFeSi and, in presence of Mn and/or Cr, α-Al(FeMnCr)Si.[19–22] In technological relevant Al–Mg–Si alloys the Si-containing phases are dominant. During casting, these particles form in the solidification interval and accumulate as interdendritic particles with a size of 5–50 μm. These particles cannot be resolved upon heat-treatment and are named constituent particles (CP). The following homogenization heat treatment leads to a spheroidization of the CP. This is of special importance if large, needle-shaped β-AlFeSi are formed. During prolonged aging they transform into spheroidized α-AlFeSi[19] which reduce the high temperature flow stress during hot working.

After casting, a small fraction of Fe and larger amounts of alloying elements such as Mn, Cr, Zr, V or Mo can sustain in the super-saturated grains of α-Al.[23–34] Throughout homogenization, the super-saturation leads to the precipitation of 20–400 nm sized particles, named dispersoids due to their incoherent interface and stability up to the solidus temperature.[23–25] Therefore, these elements are further referred to as dispersoid forming elemtens (DFE). In case of Mn and Cr, the dispersoids are linked to the α-Al(FeMnCr)-Si-phase showing cubic or hexagonal crystallographic structure of complex and variable composition. Although incoherent to the surrounding α-Al matrix,[26] their precipitation sequence is described as a heterogeneous nucleation mechanism at a transition phase, the U-phase, that forms during heating up between 100 °C to 350 °C on β'-Mg_9Si_5 precipitates.[24] In Zr containing alloys the coherent $L1_2$ Al_3Zr-phase is formed *via* homogeneous nucleation, with the peak transformation rate between 400 °C and 500 °C.[27] The addition of V leads to the formation dispersoids between 465 °C and 530 °C with the composition of $Al_{21}V_2$.[31] In presence of Fe additional dispersoids with V incorporation into α-AlFeVSi type phases have been found in.[32] The $Al_{21}V_2$ phase is reported to be of cubic structure with an incoherent interface to the surrounding matrix, however, a precipitation mechanism has not yet been described. Mo has been found to form dispersoids of Al(Fe,Mo)Si-type above 500 °C in,[33] however, lacking description of crystal structure and precipitation mechanism during homogenization, due to its current minor technological importance for aluminum alloys. The discussed DFE can also be incorporated into CP during casting, therefore, DFE can influence the formation of CP.

Both CP and dispersoids affect the microstructure and texture formation although inversely. During working larger CP are broken down to smaller particles. However, their size remains in the range of 1–10 μm, thus being much larger than dispersoids. In sheet forming during cold rolling,[13] deformation accumulates in the vicinity of the CP, locally increasing the dislocation density. If the driving force for recrystallization is exceeded, subsequent annealing leads to particle stimulated nucleation (PSN) of deformation free, recrystallized grains.

Small but closely distributed dispersoids hinder the grain migration during grain growth by grain boundary pinning. The pinning pressure p_{SZ} of the so-called Smith–Zener drag mechanism of evenly distributed spherical particles of volume fraction f_v and a median particle radius r on a grain boundary with a grain boundary energy of γ_{gb} is defined in Eq. [1].[35,36]

$$p_{SZ} = \frac{3 f_v \gamma_{gb}}{2r}. \qquad [1]$$

It is evident that in the same material system, where γ_{gb} can be assumed as constant within the compositional boundaries, the pinning pressure increases with higher dispersoid volume fraction and smaller particle size.

Besides the deformation mechanism of the material, the third factor regards the external parameters of deformation, which are the applied strain state and the working temperature. Increasing the total strain and temperature promote recrystallization and grain growth. In case of plane strain deformation during Al sheet rolling at low temperatures, the resulting deformation texture described by texture components of the β orientation fiber. By approximation, this plane strain state can also be found in the extrusion of bands and plates of Al alloys.[9,37] In contrast to that, the extrusion of round bars shows a rotational symmetry leading to the formation of a fiber texture, where the $\langle 111\rangle$ and $\langle 001\rangle$ poles are oriented parallel to the extrusion direction.[38]

A large difference from extrusion to sheet rolling, however, lies in the temperature control during working. In sheet rolling, the material is incrementally deformed over several passes through rolls at either cold or hot temperatures,[4,12,15] with optional temper heat treatments in-between rolling passes. In this manner, the microstructure evolution by deformation and recrystallization can be controlled incrementally in each processing step. By contrast, hot deformation and shape forming happen simultaneously and within a brief period during extrusion, leading to high strain rates with locally varying strain states, depending on profile geometry and position on the profile. The friction

between the tool and the material flow becomes increasingly important and results in a shear strain state towards the surface of the profile.[39,40] Such shear deformations result in different texture components, which also were observed in extrusion profiles.

The high strain rates during extrusion lead to an increase in material temperature under deformation. Together with the high total strain this results in a high driving force for recrystallization. Although discontinuous dynamic recrystallization by nucleation and growth is only expected for low stacking fault fcc materials, two mechanisms of dynamic recrystallization have been reported for hot deformation of Al alloys.[41–51] One mechanism is the continuous dynamic recrystallization (CDRX) where low angle grain boundaries of subgrains are transformed into high angle grain boundaries by accumulating dislocations during deformation. The other mechanism is the geometric dynamic recrystallization (GDRX) that occurs at large strains when grains reduce to 1–2 subgrains, so that opposing high angle grain boundaries can come into contact and split the original grain. Such microstructures have relatively high stored energy, and their crystallographic texture resembles that of the deformed state.[52]

When recrystallization annealing follows cold rolling, the resulting recrystallized texture for fcc alloys deformed under plane strain shows Cube $\{100\}\langle 001\rangle$ texture component.[4,10,28,53,54] The mechanism of formation is explained as preferential growth of Cube oriented nuclei, located in Cube bands that are present after deformation. These nuclei have lower energy than the surrounding matrix of grains of β orientation fiber due a larger subgrain size, leading to a large driving force for grain growth. Additionally, the misorientation between the Cube component and the S component of the β-fiber is close to the highly mobile $40\text{deg}\langle 111\rangle$ grain boundary misorientation, supporting the early growth of Cube grains.[51,54–56]

The surface area of the profile experiences high deformation during the extrusion process in a shear zone between the dead metal zone and the billet, and upon exit between the profile and the die orifice.[57,58] . This leads to a rise of strain and strain rates in this area, which presents a high driving force for recrystallization. For the recrystallization in the sub-surface layer, however, neither Cube texture components[9,59] nor any other distinct texture have yet been reported. If recrystallization in this layer leads to grain growth, the resulting microstructure is referred to as peripheral coarse grain (PCG). The formation of this layer is explained by van Geertruyden *et al.*[59,60] as a mechanism of abnormal grain growth of an initial microstructure of fine, equiaxed grains separated by high angle boundaries developed by GDRX, after the profile exits the die. The PCG growth is driven by the reduction of grain boundary energy and activated by the thermal energy released during deformation.[49,61] The strain state and rate, and thus the temperature in the shear layer is affected not only by the flow in the press and throughout the die, but can also be altered by the design of the die orifice, giving rise either to a larger shear zone or a pronounced PCG formation.[39,40]

The formation of the PCG layer has been discussed in the context of grain growth driven by the reduction of stored energy in a highly deformed microstructure showing small grain sizes and a deformation texture. On the other hand, deformation microstructure, recrystallization and grain growth of the bulk have been largely discussed in the framework of sheet rolling without regarding surface and sub-surface effects. Through-thickness variations have been investigated, but only in regard of gradient strain states. This study, therefore, aims to describe the relation between PCG formation and recrystallization and grain growth processes in the bulk over a variety of extruded Al–Mg–Si alloys, regarding the driving forces for recrystallization and grain growth and the influence of texture on it.

II. MATERIAL PROCESSING AND EXPERIMENTAL METHODS

A. *Industrial Sized Processing Route of Al–Mg–Si Extrusion*

As sample material five experimental alloys of the Al–Mg–Si class have been designed that aim to have a medium to high strength. Their chemical composition is listed in Table I. With increasing amount of the hardening-phase forming elements Mg, Si and Cu, the weight fraction of dispersoid forming elements (DFE) Fe, Mn and Cr was increased as well. The aim was to achieve a monotonic increase of the amount of constituent particles and dispersoids. An exception to this is alloy 6005A.CP- which was designed to contain less constituent particles than 6005A by a reduced Fe content, while retaining a similar level of dispersoids.

All alloys have been cast by Direct Chill casting into 10'' billets of 7 m length and were subsequently homogenized at 560 °C ± 20 °C for 4 hours by Hammerer Aluminium Industries Casting GmbH. After homogenization the billets have been extruded with a 41 MN servo-hydraulic extrusion press by Hammerer Aluminium Industries Extrusion GmbH. The billets were cut into blocks of 750 mm length and preheated to 490 °C before loading into the extrusion press. The blocks were then extruded into a thin-walled hollow profile with two chambers (Figure 1) with a wall thickness of 2.5 mm and a cross section area A_P of 1080 mm^2. In respect of the billet cross-section area A_B this results in a nominal extrusion ration A_B/A_P of 47 and a corresponding deformation strain $\varphi = \ln A_B/A_P$ of 3.9. The extrusions were conducted with three ram speeds to realize different strain rates during shape forming. This resulted in distinct profile exit speeds of 5, 10 and 15 m/min with profile exit temperatures of 528 °C ± 2 °C, 556 °C ± 5 °C and 570 °C ± 9 °C, respectively. The temperature was measured by a thermocouple in contact with the profile upon its exit of the press.

Table I. Composition Range in Weight Percent of Alloys

Alloy	Alloy Type EN 573-3	Al	Si	Fe	Cu	Mg	DFE (Fe + Mn + Cr)	Rest
6005	6005	bal.	0.6–0.9	< 0.35	< 0.1	0.4–0.6	0.34	< 0.15
6005A	6005A	bal.	0.5–0.9	< 0.35	< 0.3	0.4–0.7	0.52	< 0.15
6005A.CP-	6005A	bal.	0.5–0.9	< 0.05	< 0.3	0.4–0.7	0.50	< 0.15
6082	6082	bal.	0.7–1.3	< 0.5	< 0.1	0.7–1.2	0.78	< 0.15
6082 +	6082 + Cu	bal.	0.7–1.3	< 0.5	< 0.5	0.7–1.2	1.13	< 0.15

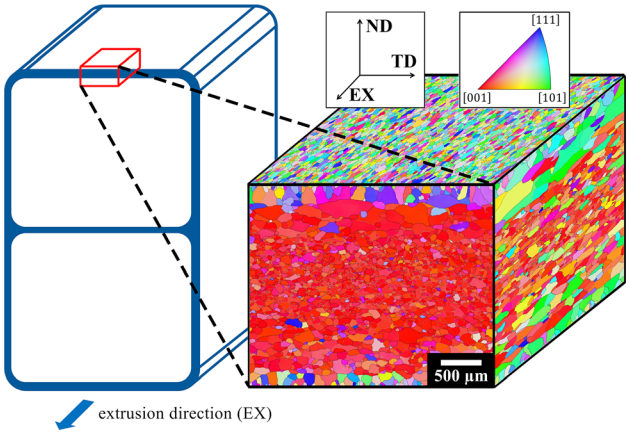

Fig. 1—Shape of the thin-walled hollow profile with the section and reference orientation for texture analysis. Color code for IPF coloring are poles normal to each acquisition plane (Color figure online).

After exiting the extrusion press the profiles were water quenched with a minimum quench rate of > 20 K/s to retain the supersaturated solid solution. As the final processing steps, the profiles were stretched, cut and stabilization heat treated after extrusion.

B. *Analysis of Dispersoids*

For microstructural analysis of the dispersoids samples from profiles extruded at moderate extrusion speed (10 m/min) were taken. The dispersoids form during homogenization and are not altered by extrusion speed or temperature. Therefore, the microstructure obtained by the moderate extrusion speed is regarded as representative for each alloy in general. The sections were made perpendicular to the extrusion direction (EX), so that the transverse (TD) and normal direction (ND) lie within the analyzed plane. The sections were embedded in a polymeric resin, ground with SiC paper to 2400 grit and consecutively polished with diamond suspensions of 6, 3 and 1 μm particle size. The final polishing step was conducted with colloidal silica of 0.04 μm particle size.

Investigations and analysis of the dispersoid distribution of each alloy were conducted following the routine of Österreicher *et al.*[25]: for each alloy, the microstructure was recorded in a total acquisition area of 1875 μm^2 in backscatter electron (BSE) contrast at 5 kV using a Zeiss 1540 EsB Crossbeam SEM. With ImageJ[62] the acquired images were filtered, binarized and measured concerning the area and size of each dispersoid. In order to obtain information on the volume fraction, the registration depth of backscattered electrons was estimated using the CASINO Monte Carlo software.[63] According to the routine proposed by Österreicher *et al.* explained in detail in[25] a dispersoid size dependent registration volume was assessed for each particle. With the assumption of spherical dispersoid particles the volume fraction of dispersoids f_v was determined for each alloy following the summation in Eq. [2] over all dispersoids with a cut-off diameter $d_{cut} < 400$ nm:

$$f_v = \sum_{i}^{i_{d_{cut}}} \frac{v_i}{V_{i,acq}} = \sum_{i}^{i_{d_{cut}}} \frac{\frac{4}{3}\pi\left(\frac{A_i}{\pi}\right)^{3/2}}{A_{acq} \cdot z_{i,reg}}, \qquad [2]$$

where v_i is the volume of an individual dispersoid, $V_{i,acq}$ is the corresponding acquisition volume, A_i is the measured area of an individual dispersoid, $z_{i,reg.}$ is its size dependent registration depth and $A_{acq.}$ the total acquisition surface.

C. *Quantification of Constituent Particles (CP)*

Constituent particles (CP) were quantified from sections of the extruded profile with orientations of 0, 25, 37, 45, 56 and 90 deg. The orientation angle describes the angle between the normal of the acquisition plane and the extrusion direction in the EX-TD-plane. The different orientation angles account for the preferred orientation parallel to the extrusion direction. Similar to the procedure used for dispersoid analysis, only the states processed at the moderate extrusion speed (10 m/min) were investigated. For each alloy and each orientation an acquisition surface of 0.75 mm^2 was recorded with backscatter electron (BSE) contrast at 12.5 kV using a Zeiss 1540 EsB Crossbeam SEM. The CP were evaluated with ImageJ[62] to obtain the area fraction for each alloy and orientation. By incorporating particle analysis under different acquisition orientations, this results in a random particle distribution, where the area fraction can be regarded as the statistical mean of the volume fraction.

In order to compare the experimentally determined fractions of CP and dispersoids with their respective theoretically possible fractions at the homogenization temperature, equilibrium thermodynamic calculations were conducted using the aluminum database in JMatPro V10.2.

Table II. Definition of Orientation Fiber Textures and Contained Texture Components with Respective Euler Angles

Orientation Fiber Texture	Texture Component	Euler Angles		
		φ_1/deg	ϕ/deg	φ_2/deg
⟨001⟩||EX	Cube	0/90	0	0/90
$\varphi_1 = 0$ deg, $\varphi_2 = 0$ deg	Goss	0/90	45/90	0/45
β-fiber	Brass	35	45	0/90
spread between Brass-S-Copper	S	59	37	63
	Copper	90	35	45
⟨101⟩||*TD*	Rotated Cube	0/90	0	45
$\varphi_1 = 90$ deg, $\varphi_2 = 45$ deg	Copper	90	35	45
	Copper-Twin	90	71	45
	Goss	0/90	45/90	0/45

Table III. Phase Fraction of Constituent Particles and Dispersoids

Alloy	Equilibrium frac./Volume Percent	Const. Particles/ Volume Percent	Dispersoids/ Volume Percent	Dispersoid Diameter/nm		
				Median	5 pct	95 pct
6005	0.69	0.38	0.11	80	33	165
6005A	1.16	0.53	0.33	71	29	156
6005A.CP-	0.83	0.26	0.39	88	22	173
6082	1.70	0.73	0.55	72	24	167
6082 +	2.58	1.1	0.82	73	24	164

D. *EBSD Measurements*

To obtain information on texture formation and grain size electron backscatter diffraction (EBSD) measurements were conducted in three planes per alloy and extrusion speed. The position of the selected specimens in the profile is drawn as a red box in Figure 1. The sections were chosen so that the normal of the investigated planes were parallel to EX, TD and the surface (ND). It is noteworthy, that directions TD and ND are defined in respect to the local specimen position where the sample was taken. Metallographic preparation consisted of grinding with SiC paper to 2400 grit, 6 μm diamond suspension polishing and final electrolyte polishing using an alcohol-based solution of 3 pct $HClO_4$ cooled to − 5 °C, polished for 5–10 seconds at 55 V. Sample preparation for the surfaces consisted solely of electrolyte polishing. For in depth analysis, measuring over a statistically representative number of grains, target grinding in ND direction was performed on selected samples.

The EBSD measurements were performed using a Zeiss 1540 EsB Crossbeam SEM with an Oxford Nordlys Nano detector. The beam step size was 3 μm for orientation analysis. The mappings in planes EX and TD had a width of 3.5 mm and a height of 2.5 mm, covering the whole wall thickness. The mappings in ND where sized to fit the measurements in the EX and TD planes. In case fine-grained microstructures could not be resolved sufficiently additional measurements limited to the fine-grained area were performed with as step size of 0.7 μm.

E. *Orientation and Texture Representation*

The EBSD measurements were used to analyze the micro- and macro-texture using the MTEX toolbox for Matlab.[64] For the micro-texture analysis inverse pole figure (IPF) maps were created for each section plane EX, TD and ND. The reference orientation for color mapping was its plane normal EX, TD and ND, respectively. Additionally, low angle (2–10 deg) and high angle (>10 deg) grain boundaries were reconstructed for each mapping. The three perpendicular IPF maps were then arranged to a microstructure cube, to resemble a cubic cut as seen in Figure 1.

For the macro-texture analysis, the orientation distribution for each alloy and extrusion speed was quantified in terms of orientation fibers and texture components. The orientation fibers and texture components of interest are listed in Table II. The quantification was performed on the unfiltered mappings due to the high indexing rate of > 95 pct. For this, the specimen orientation was centered so that the orientation distribution coincided with the plane strain deformation mirror planes. This eliminates small deviations from ideal orientation introduced during grinding and mounting in the SEM, thus being necessary for texture quantification in terms of ideal texture components defined in Table II.

The orientations of each EBSD mapping were then compared to each of the ideal texture components and fibers by means of smallest misorientation angle. An ideal orientation or orientation fiber was assigned if the misorientation was ≤ 10 deg, which ensured that ideal

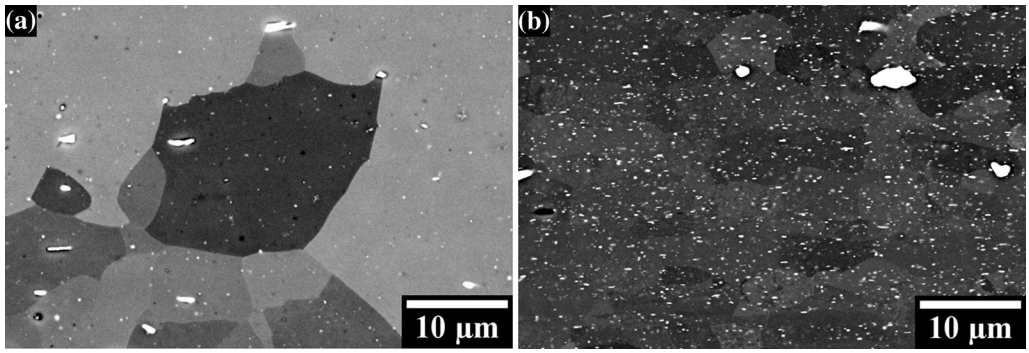

Fig. 2—Microstructure of (*a*) alloy 6005 and (*b*) alloy 6082+ showing content and distribution of intermetallic particles. Large constituent particles (> 1 µm) form during casting, whereas smaller dispersoids precipitate during homogenization heat treatment.

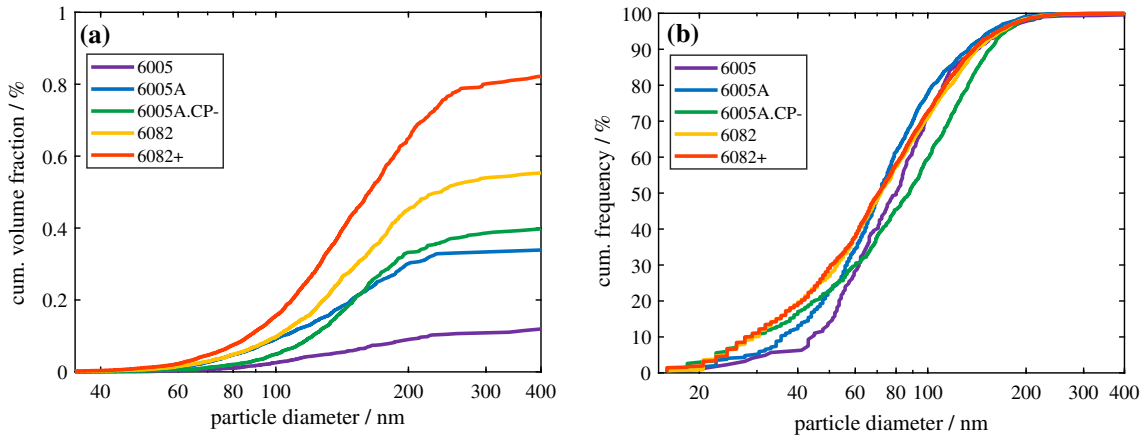

Fig. 3—(*a*) Cumulative volume fraction of dispersoids. (*b*) Cumulative frequency of dispersoids.

texture components did not overlap. Consequently, each orientation were assigned to a single ideal texture component or were defined as a random orientation. Though, this does not generally apply to orientation fibers, *e.g.*, the Goss texture component is both part of the ⟨001⟩||EX and the ⟨101⟩||TD orientation fiber. Summation over each texture component or fiber in relation to all indexed data points then yielded the fraction of each texture feature representing macro-texture of the measured cross section. Additionally, the spatial extent of the PCG layer was determined geometrically from the IPF maps in EX and TD section planes using ImageJ.

Finally, for texture and PCG layer representation of the profile microstructure, the means of the fractions of texture components from both EX and TD sections were taken.

III. RESULTS

A. *Phase Fraction of Constituent Particles and Dispersoids*

The microstructures after extrusion of the alloys 6005 and 6082+ are shown in Figure 2(a) and (b), respectively. The phase distribution can be divided into large precipitates, constituent particles (CP), with a diameter of > 1 µm, and smaller dispersoids. The constituent particles are elliptical to elongated in shape. They form during casting and are broken down during extrusion. Dispersoids are of smaller size and precipitate during homogenization. Their precipitation is aimed to result in a diameter of < 400 nm, and they exhibit a spherical to elliptical shape. In Figure 2(a) the strong grain boundary pinning effect caused by the Smith–Zener drag of the dispersoids can be clearly seen. At a closer look at the grain boundary of the dark grain in the middle, pinning along its grain boundary on dispersoids and an inwards curvature between those points is visible. This is a sign for grain growth, that is consuming the dark grain, but is counter-acted by the Smith–Zener drag. Alloy 6005 in Figure 2(a) shows a smaller dispersoid density with 0.34 pct DFE than alloy 6082+ in Figure 2(b) with 1.13 pct DFE. This shows qualitatively that with an increasing content of DFE, a higher amount of nanoscopic dispersoids are formed.

The volume fraction of dispersoids in the investigated alloys is shown in Figure 3(a). For all five alloy compositions the dispersoid volume fraction increases following a logarithmic normal distribution towards a saturation at dispersoid diameters of about 400 nm.

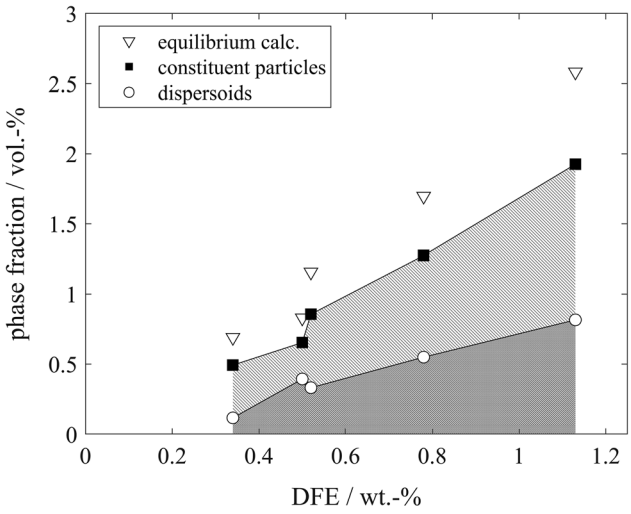

Fig. 4—Volume fractions of dispersoids and CP stacked on top of dispersoids. For comparison the theoretical equilibrium fraction of CP and dispersoid phases at extrusion temperature is given.

Although the volume fraction varies substantially between the alloys, the corresponding size distribution is relatively similar (Figure 3(b)). The cumulative frequencies of dispersoid size follows a logarithmic normal distribution with a median value for all alloys of 71–88 nm diameter. To avoid misconception, the distribution of cumulative volume fraction in Figure 3(a) accounts for the volume fraction of dispersoids and is therefore shifted to larger particle size, as small particles contribute less to overall volume fraction. By contrast, the cumulative relative frequency in Figure 3(b) regards numeric frequency, where each particle contributes equally, irrespective of its size.

The saturation at a dispersoid diameter of 400 nm in Figure 3(a) marks the dispersoid volume fraction of the alloys. The corresponding median dispersoid size for each alloy is defined by the dispersoid diameter at the median in Figure 3(b). These dispersoid values are listed in Table III together with the volume fraction of the constituent particles and the calculated thermodynamic equilibrium volume fraction. Figure 4 shows the increase in volume fraction of the equilibrium phase with increasing DFE content. The fraction of dispersoid and the CP fraction increases, accordingly. An exemption to this behavior is 6005A.CP-. It is compositionally close to alloy 6005A with a comparable content of DFE. However, due to a different casting routine and an adjusted composition of DFE this alloy shows less formation of CP during casting. This leads to an increased volume fraction of dispersoids by 18 pct to that of 6005A, as less DFE is incorporated into CP.

The offset between the sum of CP and dispersoids to the calculated equilibrium fraction in Figure 4 can be explained by the non-equilibrium state of the alloys. However, the finite resolution of SEM imaging could lead to an underestimation of volume fraction, as the smallest dispersoids < 20 nm could not be detected, although their contribution to overall volume fraction should be very small (Figure 3(a)).

B. *Evolution of Microstructure Components During Extrusion*

The microstructure at the flat section of the profile as marked in Figure 1 is displayed in Figure 5 as microstructure cubes for the five investigated alloys, each extruded at three different extrusion speeds. Each microstructure cube consists of IPF maps of sections of the EX- and TD-plane and the profile's surface as the ND-plane. Depending on extrusion speed and alloy different microstructural developments can be identified in the bulk of the cross section in the ODFs of Figure 6. Regarding the formation of microstructure in the bulk, alloy 6005 extruded at any extrusion speed, alloy 6005A extruded at 10 and 15 m/min and alloy 6005A.CP- at 15 m/min show many grains oriented along the ⟨001⟩ crystallographic axis lying parallel to the extrusion direction. On the other hand, alloy 6082+ at any extrusion speed, 6082 at 5 m/min and 10 m/min and 6005A.CP- at 5 m/min develop a dominant pole spread from ⟨211⟩ to ⟨111⟩ parallel to the extrusion direction, while retaining a small grain size. The remaining bulk microstructures in between can be described as a combination of both microstructure developments with small grains of ⟨211⟩- to ⟨111⟩-poles parallel to EX and large grains of ⟨001⟩||EX orientation.

To further describe the texture development, additionally to the microstructure cube, Figure 6 shows the orientation density function (ODF) map for φ_2-sections of 0, 45 and 65 deg of the whole cross-section of alloys 6005A (top row), 6005A.CP- (2nd row), 6082 (3rd row) and 6082+ (bottom row) extruded at 10 m/min. Figure 7 contains the texture development along the cross-section from surface to surface of the profile section in the sense of texture fiber content.

The ODF map of 6005A (Figure 6, top row) shows that its texture is dominated by the Cube texture component with a small spread of orientation to the Goss component. This is in line with the fiber description as ⟨001⟩||EX. This texture is associated with recrystallization texture of aluminum under plane strain and can be explained by the small amount of dispersoids in this alloy, thus exerting the smallest Smith–Zener drag on migrating grain boundaries enabling grain growth. However, global ODF does not sufficiently describe the local micro-texture and the through-thickness variation of orientation. Next to the bulk microstructure the peripheral coarse grain layer forms. This layer can be distinguished from the bulk texture in the TD plane of the microstructure cubes with ⟨101⟩||TD oriented grains (Figure 7(a)). The distribution of texture fiber content along the cross-section consequently results in a dominant ⟨001⟩||EX-fiber in the bulk while the PCG layer is defined by the ⟨101⟩||TD-fiber. It must be noted, that at 400 μm depth both fibers add up to > 100 pct. This is due to the Goss texture component being part of both fibers.

The highly alloyed 6082+ (Figure 6, bottom row) globally displays a more homogenous distribution in the microstructure cube. The corresponding ODF shows a dominant β-fiber orientation with a strong peak at the Brass component and decreasing intensity over the S

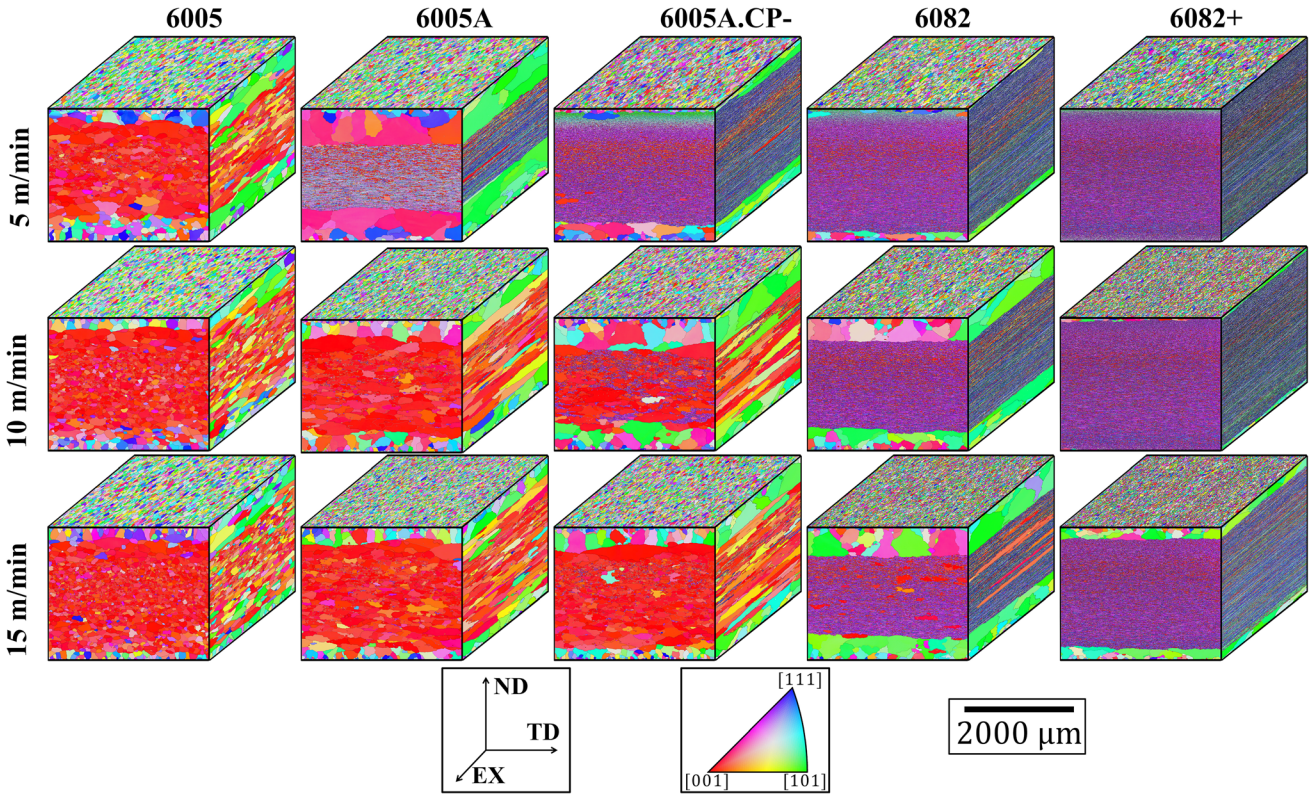

Fig. 5—Microstructure and texture evolution of the extrusion alloys at different extrusion speeds. The microstructure cubes show the microstructure normal to the EX-, TD- and in the ND-plane as the surface. The grains are colored in IPF coloring, with respect to their poles parallel to the acquisition plane normal (Color figure online).

component to the Copper component, while the maximum overall intensity is smaller than that of 6005A. This is coherent with the observation from the microstructure cubes in Figure 5, which show the ⟨211⟩- to ⟨111⟩-poles parallel to EX. This β-fiber texture describes a deformation texture under plane strain in Al alloys.

The high amount of dispersoids in alloy 6082+ leads to a strong pinning of grain boundaries, effectively reducing grain boundary migration, resulting in a fine-grained microstructure with thin grain layers partially consisting of only one subgrain in height. A very thin PCG layer can be observed in the microstructure cube, but the intensity is too weak to be found in the ODF map. However, the cube component shows a weak but noticeable intensity in the ODF. This is reflected in the fiber orientation distribution for 6082+ (Figure 7(d)). The PCG layer only leads to a high fraction of ⟨101⟩||TD-fiber just few tens of microns beneath the surface. The remaining cross-section is dominated by the β-fiber orientation in the bulk. The weak intensity related to the Cube component can be found at a depth of 750–1000 μm beneath the surface with a local maximum of the ⟨001⟩||EX-fiber orientation. This local maximum correlates with a local minimum of the β-fiber, indicating that these bulk fiber orientations behave complementary. At a depth of 2300 μm a local maximum appears in the ⟨101⟩||TD-fiber and adds up to $>$ 100 pct together with the β-fiber. This is associated to the formation of the Copper component, which can be assigned to both fiber orientations.

Alloy 6082 extruded at 10 m/min (Figure 6, 3rd row) shows a higher number of local peaks in its global ODF map. The overall intensity is smaller than that of 6005A and 6082+, but similar to 6082+ the strongest intensity can be located at the Brass component with decreasing intensity to the S and the Copper component. However, additional peaks appear in the ODF map along the line of the Euler angles $\varphi_1/\phi/\varphi_2 = 90\,\text{deg}/x/45\,\text{deg}$, describing the ⟨101⟩||TD-fiber. The fiber orientation distribution along the cross section (Figure 7(c)) shows, that this fiber orientation is once more associated with the PCG layer. Its ODF reveals that, alongside with the Goss and Copper texture component, the strongest intensities of the ⟨101⟩||TD-fiber are found at the Rotated Cube and the Copper Twin texture component. In between the PCG layers the bulk is defined by a sharp decrease of the ⟨101⟩||TD-fiber content and a dominant β-fiber fraction, comparable to 6082+. In contrast to 6082+, the fraction of ⟨001⟩||EX-fiber increases for 6082. Due to this complementary behavior of the fiber's texture components the maximum β-fiber fraction is reduced.

The microstructure cube of 6005A.CP- (Figure 6, 2nd row) shows a large PCG layer comparable to 6082, as discussed above. The bulk shows large grains of ⟨001⟩||EX-fiber orientation separated by a small fraction of small β-fiber oriented grains. According to this, the ODF shows a large extent of ⟨001⟩||EX-fiber with a

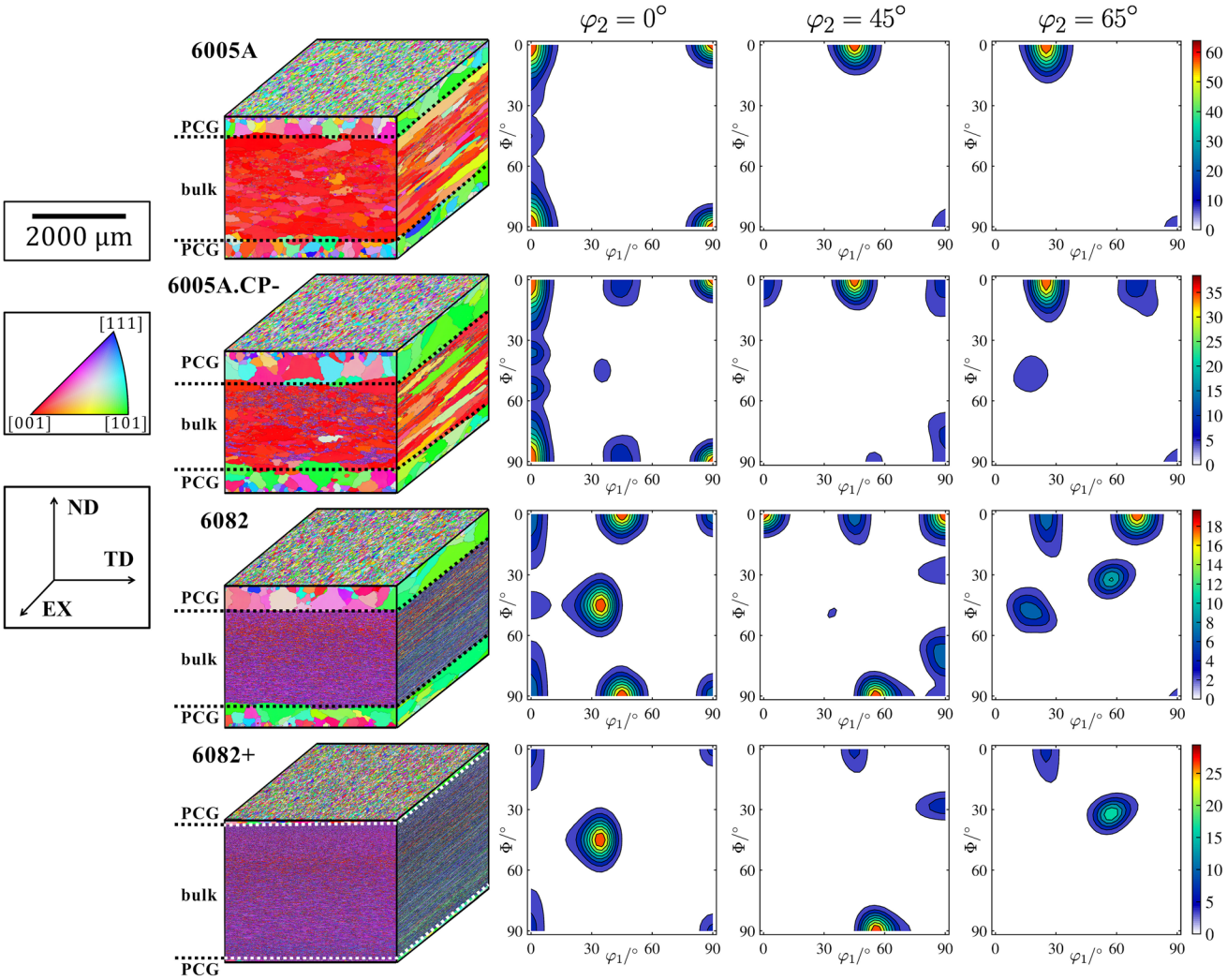

Fig. 6—Microstructure cubes, orientation density function (ODF) maps for alloys 6005A, 6005A.CP-, 6082 and 6082+ at 10 m/min extrusion speed. The microstructure cubes show grain and texture distribution within the profile in the PCG layer and the bulk. ODF maps of EX direction in φ_2-sections of 0/45/65 deg represent the macro texture.

strong Cube texture component, a minor peak at the Brass component and a split of ⟨101⟩||TD-fiber into Rotated Cube and Copper Twin component.

This separation of grain sizes in the bulk with their corresponding fiber orientations describes the transition microstructure between none and extensive grain growth of ⟨001⟩||EX oriented grains. While in the bulk two kinds of microstructures can develop, the PCG layer is described by the development of the ⟨101⟩||TD-fiber in the global ODF. The through-thickness transition from the PCG layer to the bulk is visible as a less steep slope in the orientation fiber fraction distribution (Figure 7(b)) at 500 − 600 μm due to the formation of the Goss texture component, that is part of the ⟨001⟩||EX as well. Additionally, the grains of the PCG layer and the ⟨001⟩||EX oriented grains in the bulk are of comparable size. This leads to a less even and planar boundary between PCG layer and bulk.

Therefore, the bulk and PCG layer can be distinguished by the fiber components. In addition to that, the bulk can be characterized regarding the two fiber orientations ⟨001⟩||EX and β. Figure 8 shows the fraction of microstructure components over the whole cross section of each alloy extruded with 5 m/min (left), 10 m/min (middle) and 15 m/min (right). With increasing extrusion speed the deformation rate increases, leading to higher strain rates and higher temperatures of the extrusion profile. This increases the grain boundary mobility that enables grain growth. The strain distribution over the cross section, that affects the stored energy and thus the driving force for grain growth, however, is expected to stay relatively constant for the different extrusion speeds. In Figure 8 the alloys are arranged in the order of increasing dispersoid content and hence grain boundary pinning effect, which counteracts the grain boundary mobility. The amount of the PCG layer is characterized by its depth over the cross section and texture information. The microstructure composition in the bulk is shown as ⟨001⟩||EX- and β-fiber fraction, describing the coarse-grained and fine-grained microstructure, respectively. For all investigated microstructures there is only a very small amount

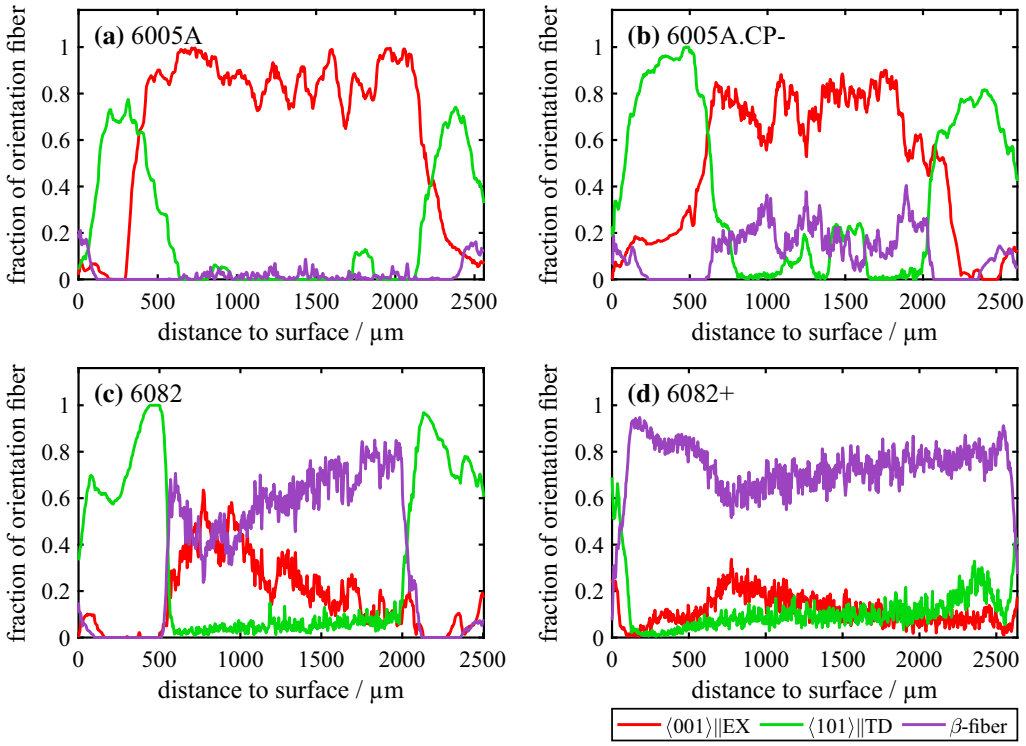

Fig. 7—Orientation fiber distribution over wall thickness for alloys (*a*) 6005A, (*b*) 6005A.CP-, (*c*) 6082 and (*d*) 6082+ at 10 m/min extrusion speed. The fiber distribution shows the development of ⟨001⟩||EX-, ⟨101⟩||TD- and *β*-fiber content over the wall thickness.

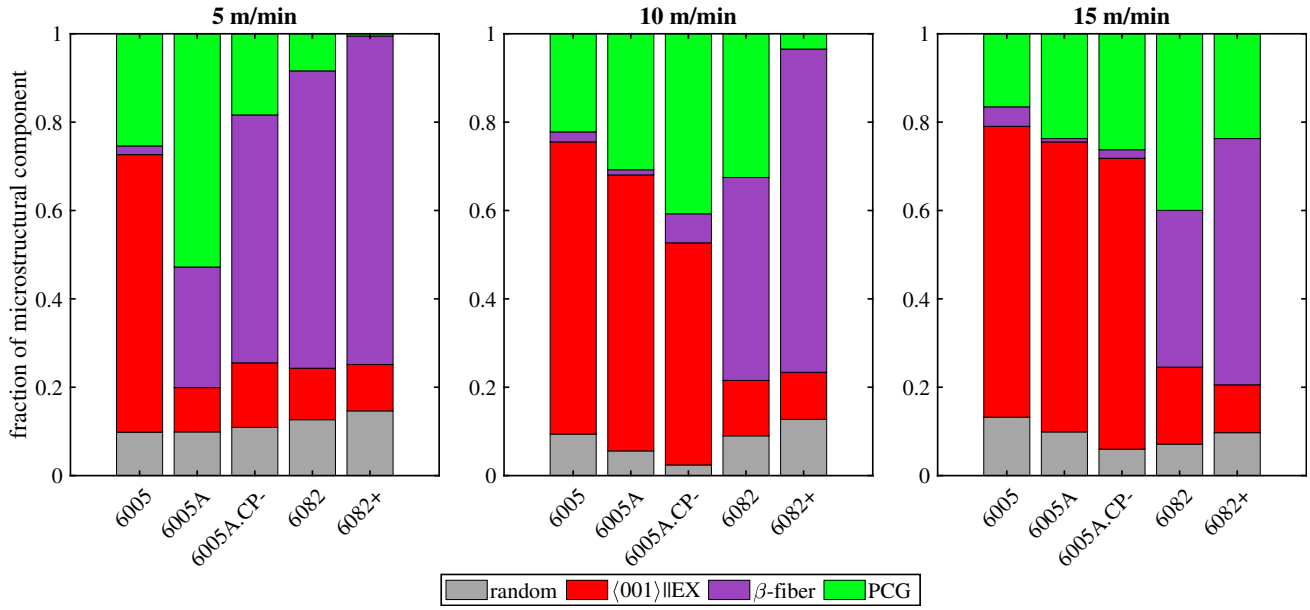

Fig. 8—Fraction of microstructural zones of PCG and bulk, with the bulk content separated into fractions of ⟨001⟩||EX- and *β*-fiber, of Al–Mg–Si alloys extruded at 5, 10 and 15 m/min.

(< 15 pct) of random orientation in the bulk that is not part of any of the two orientation fibers. This emphasizes the strongly textured nature of the investigated alloys upon extrusion shape forming.

At the low extrusion speed of 5 m/min and hence small deformation rates all alloys, except for 6005, exhibit *β*-fiber in the bulk (Figure 8, 5 m/min). The amount of ⟨001⟩||EX-fiber stays constant at an overall fraction between 10 and 15 pct. While in alloy 6082+, with the highest dispersoid content, nearly no PCG forms, the extent of PCG increases with reducing dispersoid content. The largest PCG size at this extrusion speed is reached in 6005A. Further reduction of the amount of dispersoids in 6005 does not increase the size

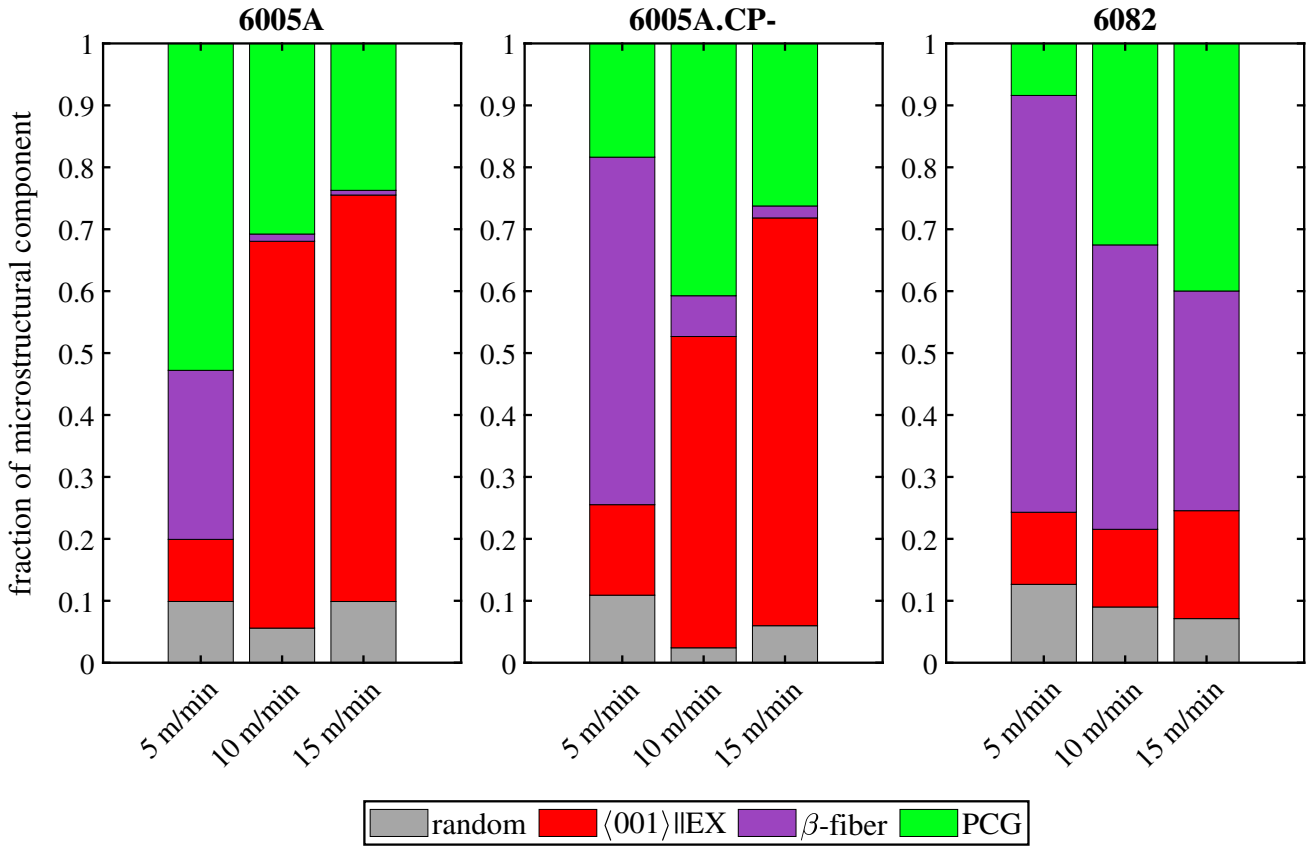

Fig. 9—Fractions of microstructural zones from Fig. 8, showing the development of microstructural zones with increasing extrusion speed for alloys 6005A, 6005A.CP- and 6082.

of the PCG layer but increases the fraction of ⟨001⟩||EX-fiber in the bulk at the expense of the β-fiber, which is not present in this microstructure.

With an increase of the extrusion speed to 10 m/min (Figure 8, 10 m/min) or to 15 m/min (Figure 8, 15 m/min), the largest PCG is observed in 6005A.CP- and 6082, respectively. At these speeds the bulk of 6005A and 6005A.CP- changes to a coarse-grained ⟨001⟩||EX-fiber microstructure. In 6082 and 6082+ the fraction of fine-grained β-fiber-oriented microstructure in the bulk is reduced and the extent of PCG grows. It is noteworthy that when the bulk microstructure is mainly occupied by the β-fiber microstructure, the fraction of ⟨001⟩||EX-fiber in the bulk stays constant at a level of 10−15 pct.

To further demonstrate the effect of the dispersoid content, deformation rate and temperature on the formation of microstructural components, Figure 9 shows the evolution of microstructure with increasing extrusion speed for the three alloys 6005A, 6005.CP- and 6082. The increase in extrusion speed increases the profile temperature, which leads to a higher grain boundary mobility. In alloy 6082, with a dispersoid volume fraction of 0.55 pct, the increasing grain boundary mobility affects the growth of the PCG layer to the expense of the β-fiber in the bulk.

In alloy 6005A the grain boundary mobility is already high enough for the formation of a large PCG layer, because the smaller dispersoid volume fraction of 0.33 pct results in a less effective grain boundary pinning. However, the pinning in the bulk is large enough to suppress the growth of a coarse-grained ⟨001⟩||EX-fiber microstructure. Only with higher extrusion speeds the grain boundary mobility is increased so that a coarse-grained ⟨001⟩||EX-fiber microstructure in the bulk can form. Additionally, this has the effect that the PCG layer is of smaller dimension, reducing from a fraction of 0.53 at 5 m/min to 0.31 at 10 m/min and 0.24 at 15 m/min. Alloy 6005A.CP- has a volume fraction of dispersoids of 0.39 pct, which is between alloys 6005A and 6082. Moreover, it shows a smaller amount of CP, decreasing the number of sites for particle stimulated nucleation. Consequently, the fraction of microstructural components at 5 m/min lies between 6005A and 6082. Comparable to 6082 the PCG grows larger at 10 m/min extrusion speed, due to the increased grain boundary mobility. Additionally, growth of coarse ⟨001⟩||EX oriented grains already started in the bulk, leaving only a small fraction of β-fiber microstructure in the bulk. At the highest extrusion speed of 15 m/min the fraction of ⟨001⟩||EX microstructure increases further while the amount of PCG decreases.

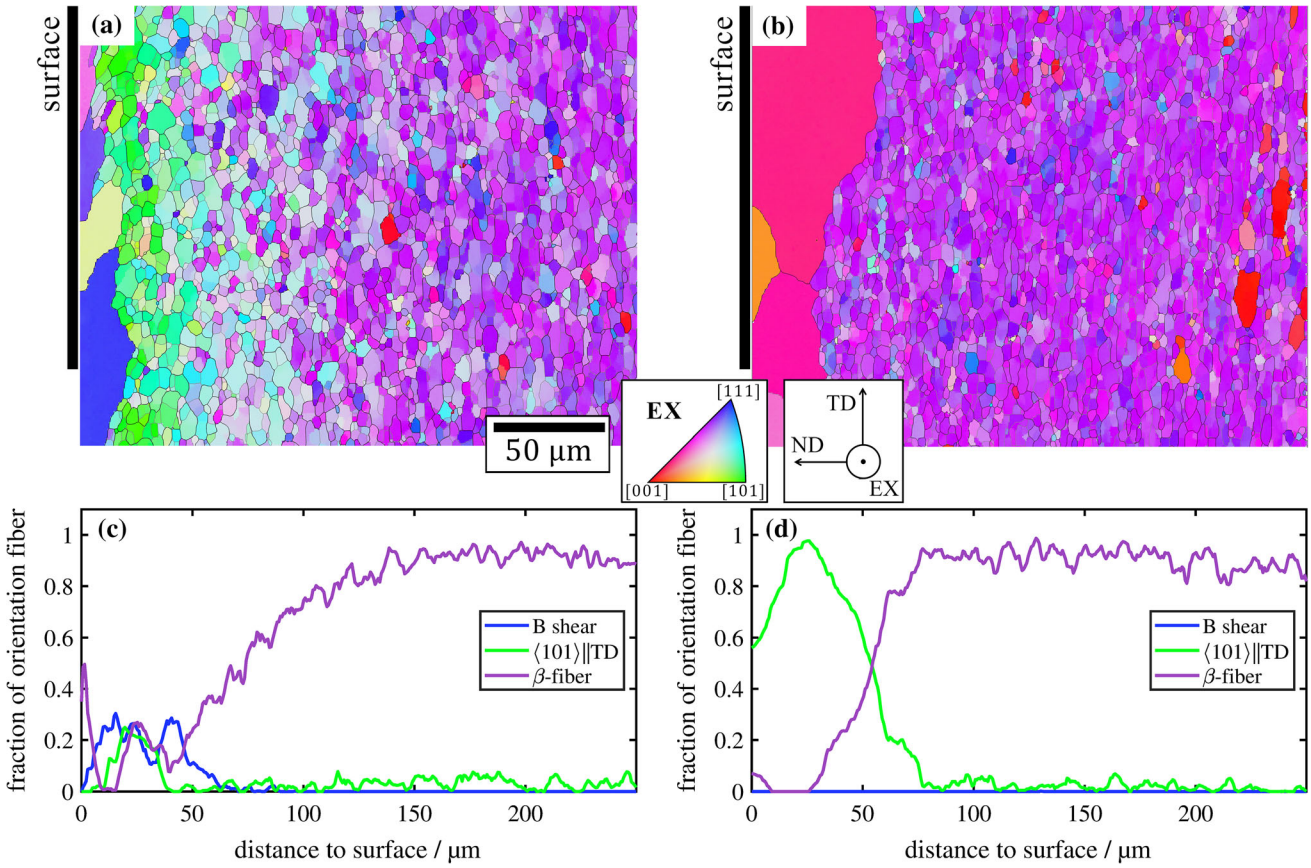

Fig. 10—Sub-surface microstructure of 6082+ extruded at (*a*) 5 m/min and (*b*) 10 m/min as IPF map color-coded in respect of EX. The orientation fiber profile relative to the distance to the surface of 6082+ at 5 m/min extrusion speed is shown in (*c*) and for 6082+ at 10 m/min in (*d*), respectively (Color figure online).

The microstructural investigation shows that with increasing extrusion speed and reducing dispersoid content at first the PCG grows, consuming a large amount of the β-fiber bulk. The formation of the $\langle 001 \rangle || \text{EX}$-fiber in the bulk then hinders further growth of the PCG layer into the bulk and counteracts its extensive growth. The formation of microstructure is dependent on the grain boundary mobility affected by the extrusion speed and temperature and the pinning pressure exerted by the dispersoids due to the Smith–Zener drag. However, the PCG growth cannot be regarded independently of the microstructural evolution in the bulk.

C. *Sub-surface Microstructure and Texture*

From Figure 8 it is obvious, that alloy 6082+ shows the highest resistance against grain growth, both in the bulk and the PCG layer. The microstructure of the cross-section extruded with a speed of 5 m/min shows few to no formation of a PCG layer. With increasing extrusion speed, however, a PCG layer grows sub-surface at the expense of the β-fiber in the bulk.

Figure 10(a) shows the sub-surface layer of 6082+ extruded at 5 m/min in the TD-ND plane, the orientations are colored according to the poles parallel to EX. Few larger grains form at the immediate surface without a specific texture. Going further into the material, a layer of small grains forms at a depth of 10 to 50 μm (Figure 10(c)), that exhibit an orientation close to $\varphi_1/\phi/\varphi_2 = 51\,\text{deg}/66\,\text{deg}/63\,\text{deg}$ or $\{211\}\langle 101 \rangle$, respectively. This orientation is also referred to as the B shear component.[65] With increasing depth, the orientation of the grains gradually transitions to the β-fiber orientation of Brass and S texture components. The misorientation relation between the B shear component and the Brass and the S texture component, respectively, is 30 deg for both, but the rotational axis is [111] for Brass, which lies parallel to TD, and [3 2 12] for the S component, which is oriented diagonally in the EX-TD-ND coordinates. The gradual transition from the B shear component to the β-fiber by gradual rotation around their rotational axes is reflected in Figure 10(c). Texture components are defined as orientations within a misorientation of 10 deg. As B shear is about 30 deg misoriented to the β-fiber orientation, an interval of 10 deg in orientation space is not regarded between B shear and the β-fiber, so that the component fraction in Figure 10(c) cannot add up to 100 pct.

The microstructure of 6082+ extruded at the increased extrusion speed of 10 m/min shows more PCG formation in Figure 8, albeit with 3.5 pct to a small extent overall. The sub-surface microstructure shows the formation of large, recrystallized grains at the immediate surface (Figure 10(b)). From the sample's orientation profile

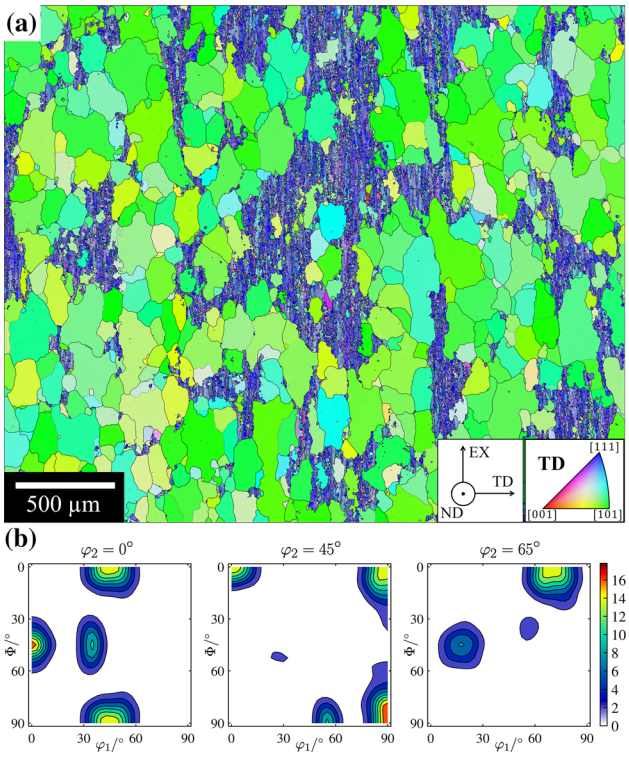

Fig. 11—(*a*) IPF map of 6082+ extruded at 10 m/min in a depth of 50 μm to the surface, color-coded in respect to TD. (*b*) shows the corresponding ODF in φ_2-sections of 0/45/65 deg (Color figure online).

(Figure 10(d)) it is evident, that no B shear component forms. The grains of the PCG layer belong to the ⟨101⟩||TD fiber. There is no gradual transition to the fine microstructure, but the β-fiber-oriented grains border abruptly to the PCG layer with increasing distance to the surface. Because the boundary between PCG layer and fine-grained microstructure is not parallel to the surface but uneven, the transition from PCG to fine-grained microstructure appears gradually in the texture profile in Figure 10(d). This boundary area lies 50 ± 20 μm beneath the surface. Figure 11(a) shows the microstructure of this boundary region in the EX-TD plane in 50 μm depth to the surface. The IPF map shows large, recrystallized grains of the PCG with a ⟨101⟩||TD fiber orientation and fine grains with an elongated shape in EX with ⟨111⟩-poles aligned parallel to TD. The ODF of this IPF map (Figure 11(b)) reveals that the fine-grained microstructure exhibits Brass component and the preferential orientation of PCG grains can be related to a composition of Rotated Cube, Goss and Copper Twin orientations. Between the latter two the ODF exhibits a spread rather than discrete peaks.

IV. DISCUSSION

A. *Influence of Grain Boundary Mobility on Microstructure and Texture*

The alloy composition and extrusion speed influence the formation of distinct microstructures and textures. From Table III it becomes clear, that with an increase in DFE the volume fraction of dispersoids increases, while the median radius stays constant. This leads to a monotonic increase of the Smith–Zener drag pressure with increasing amount of DFE. This behavior is shown in Figure 12(a). As a consequence, this enables a more effective pinning of grain boundaries during extrusion. With increasing extrusion speed the global strain rate subjected to the material increases analogically, which in consequence rises the material temperature due to adiabatic heating. However, the local strain states can vary strongly both over the profile cross section as well as across the wall thickness. These strain states can only be determined numerically by material flow simulations. However, besides the necessary software, this requires a digital model of the extrusion tool geometry as well as a parameterized material model for each alloy to calculate the flow stresses and the resulting friction, which were not available for the present investigation. Therefore, in order to ensure comparable strain states the identical position on the profile was chosen for the microstructure analysis.

The increase in strain rate leads to an increase of profile temperature after exiting the extrusion die orifice. This eases thermally activated processes such as recovery of dislocations through climbing as well as grain boundary mobility. Dislocations accumulate into grain boundaries as described by CDRX and GDRX, which results in a fine-grained microstructure that determines the stored energy in the form of the grain boundary density. This in turn is associated with the strain distribution over the profile cross section and is expected to be relatively constant and independent of the extrusion speed. The thermally increased grain boundary mobility then enables grain growth following the driving force to reduce the stored energy. The balance between the driving forces for grain growth and the counter-acting pinning pressure result in characteristic microstructures represented by microstructure cubes displayed in Figure (5).

The highest pinning pressure is exhibited by 6082+ which also shows the highest dispersoid content. Therefore, the microstructure in the bulk consists of elongated grains of β-fiber orientation at all extrusion speeds (Figures 10(a) and (b)). The formation of such a fine-grained microstructure can be explained by the mechanisms of CDRX or GDRX. Although the differentiation between both is difficult, GDRX appears to be most likely. This is concluded because EBSD-measurements show that most grains exhibit a thickness of only 1-2 subgrains and the characteristic deformation texture is preserved. Additionally, without further regard of any superimposed shear strains, the nominal deformation strain φ of 3.9 alone exceeds the critical strain of 2.5 at which GDRX has been reported to occur.[47,48]

Due to the relationship between grain structure and texture, the microstructure can be quantified by means of fraction of β-fiber orientation. In this fiber, orientations concentrate at the Brass component and show a spread over the S component, but only little of the Copper orientation component can be detected. Additionally, the formation of 10–15 pct Cube and ⟨001⟩||EX oriented grains is consistently found together with the

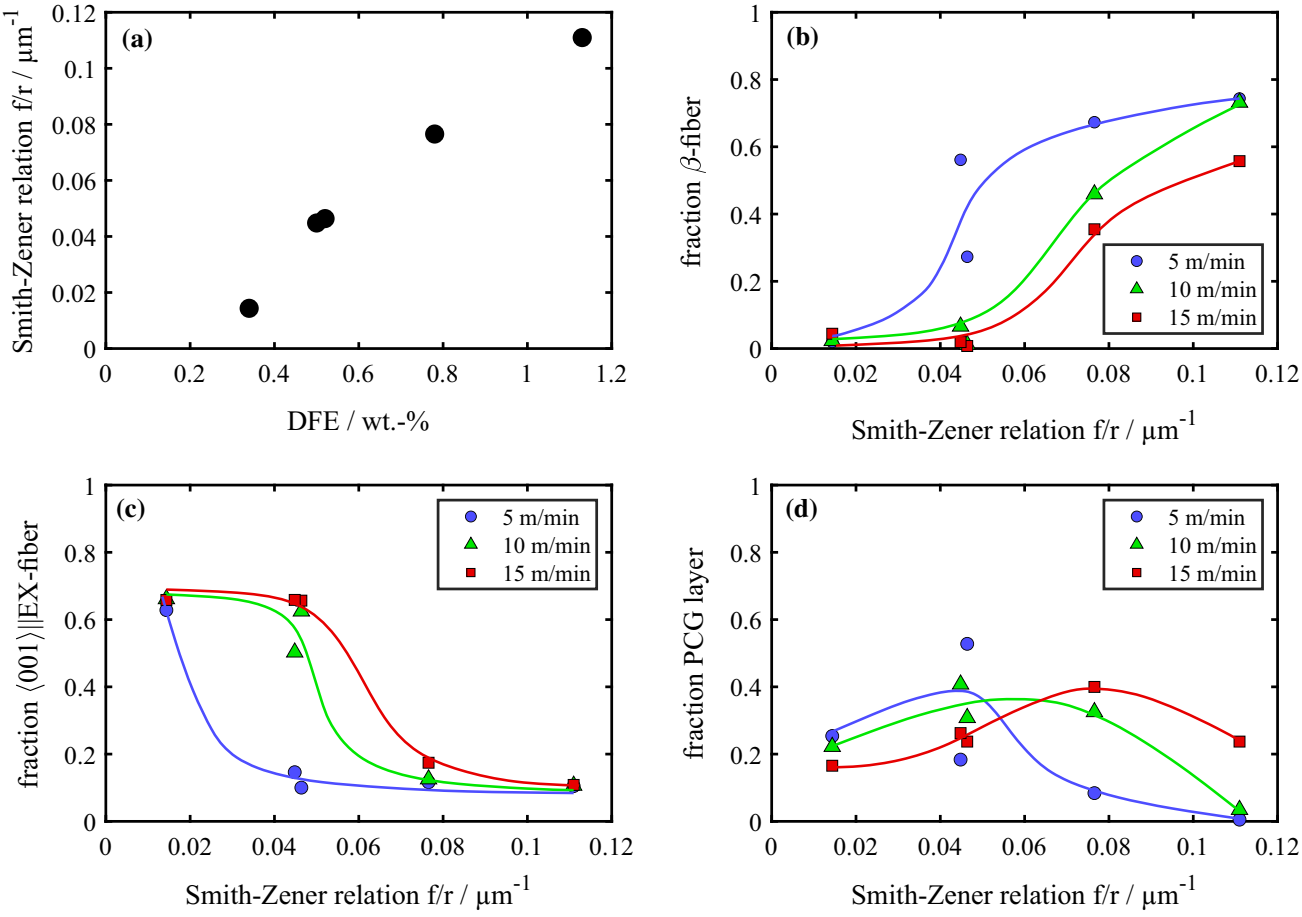

Fig. 12—(*a*) Smith–Zener relation f/r of the investigated alloys, representing the pinning effectiveness of dispersoids, in dependence of DFE content. Fraction of (*b*) β-fiber orientation, (*c*) ⟨001⟩||EX-fiber orientation and (*d*) PCG layer in dependence of Smith–Zener relation.

β-fiber orientation. The pronounced Brass formation as well as the small amount of Cube orientation is explained by activation of additional slip systems on the {110} and {100} planes during plane strain deformation at elevated homologous temperatures.[66–68]

Figure 12(b) shows the dependence of the β-fiber content in the bulk in dependence of the Smith–Zener relation for the extrusion speeds 5, 10 and 15 m/min. This relation is a measure of the grain boundary pinning effectiveness of dispersoids in the alloy system independent of the exact grain boundary energy (c.f. Eq. [1]), which depends on the misorientation between two grains. It is evident that a higher grain boundary pinning effect leads to a larger fraction of the deformation texture. However, the retained level of deformation texture is reduced by the increasing extrusion speed, due to a higher profile exit temperature, which promotes grain growth through enhanced grain boundary mobility. This enhanced grain boundary mobility affects the bulk in such a way that Cube oriented grains in Cube bands, formed during extrusion by the above explained mechanism, show preferential growth into the deformed microstructure due to high crystallographic symmetry. Besides less stored energy in Cube grains, preferential growth is supported by a near 40 deg misorientations around ⟨111⟩ of the Cube orientation to a large fraction of orientations of the β-fiber.[28,51,54–56,69] This applies to misorientations close to Σ7 grain boundaries, which pose a high mobility under growth conditions, although a slight deviation from the ideal 38.2 deg tilt misorientation around ⟨111⟩ of the highest mobility.[70] The fraction of ⟨001⟩||EX orientated grains, which incorporate Cube and Goss orientation components, as well as the spread in between, is shown in Figure 12(c) in dependence of the Smith–Zener relation. Here, an inverse relation between the fiber content and the pinning effect on grain boundaries can be observed. The fraction of ⟨001⟩||EX orientated grains increases with higher thermal activation of grain boundary mobility, due to the higher extrusion speed. However, the behavior of the contents of ⟨001⟩||EX and the β-fiber are not complementary, as they do not add up to 100 pct. This is due to the formation of the PCG layer, which to a large extent forms at intermediate pinning pressures (Figure 12(d)). With increasing extrusion speed, the peak of PCG layer fraction is shifted towards a higher pinning effectiveness. That means, that PCG formation can be suppressed by shifting the balance of driving and counter-acting forces to either extensive grain growth of Cube grains in the bulk or to high grain boundary pinning effectiveness due to dispersoids.

From the microstructure cubes (Figure 5) and their components (Figures 8 and 9) it becomes obvious, that with high pinning effects in 6082 and 6082 + the PCG layer grows deeper into the β-fiber microstructure with increasing grain boundary mobility, due to thermal activation. The content of $\langle 001\rangle||$EX oriented grains in the bulk remains constant, only for 6082 at 15 m/min the formation of larger grains of such orientation can be observed. This indicates that the grains in the PCG layer have a higher grain boundary mobility than that of Cube and other $\langle 001\rangle||$EX oriented grains in the bulk. This can be explained by friction between the material and the extrusion tool during material flow. This friction leads to a shear strain in the vicinity of the surface, which adds to the global plane strain deformation, that increases the adiabatic heating and thus the thermal activation of grain boundary mobility further compared to the bulk. The presence of shear strain underneath the surface also affects the microstructure evolution in alloys 6005A and 6005A.CP- at 5 m/min and 10 m/min. While the microstructures of both alloys at 5 m/min exhibit the dominating β-fiber microstructure in the bulk, a PCG layer forms beneath the surface, which is smaller for 6005A.CP- with a comparable Smith–Zener relation but smaller amount of CP, which promote recrystallization. Increasing the extrusion speed to 10 m/min rises grain boundary mobility in the bulk so that grains of Cube and $\langle 001\rangle||$EX orientations can grow into the surrounding β-fiber grains. In 6005A this results in the $\langle 001\rangle||$EX microstructure taking up the whole bulk and reducing the PCG extent, compared to the state at 5 m/min. In 6005A.CP- $\langle 001\rangle||$EX oriented grains are dominating in the bulk, but β-fiber microstructure is not completely consumed yet. Therefore, for this alloy the PCG layer has the largest dimension in this state. Further increase in extrusion speed to 15 m/min and thus temperature increase the fraction of $\langle 001\rangle||$EX grains and further reduces the PCG layer dimension.

B. *Selective Grain Growth of* $\langle 101\rangle||$*TD Oriented Grains in the PCG Layer*

With the growth of the PCG layer, a selection of specific orientations is evident, together with an increase in grain size from the surface towards the bulk. Hence, the mechanism of grain growth in the PCG layer appears to be of orientation selection of specific orientations during grain growth into the β-fiber textured bulk of grains with either Rotated (45 deg||ND) Cube, Goss or Copper Twin orientation, that originate in the surface or sub-surface layer. These orientations share the common crystallographic axis orientation $\langle 101\rangle||$TD.

The Rotated Cube component has been reported as a characteristic shear deformation texture component apparent in aluminum, together with the B shear orientation.[65] However, this shear deformation texture relates to lattice rotation upon deformation. Such shear deformation at elevated temperature is expected to form small grains by means of the GDRX mechanism, which is applicable only to the B shear orientation in the investigated alloys. Goss and Copper Twin components have so far not been associated with shear deformation texture. The increasing grain size in the PCG layer towards the bulk appear to follow a mechanism of orientation selection of those orientations. This can be explained by the nucleation of grains at the immediate surface, which is only weakly textured. After the profile exits the die orifice, the grains of Rotated Cube, Goss or Copper Twin orientation grow perpendicular to the surface through the shear deformed zone into the β-fiber textured microstructure. The parallel alignment of the boundary between the bulk and the PCG layer emphasizes the orientational relation of the PCG layer growth. While the driving force for the coarse grain growth can be clearly identified as the reduction in grain boundary energy of the fine-grained β-fiber microstructure, the reason for the selection of orientations of $\langle 101\rangle||$TD relation is not clear, as extensive growth of such oriented grains have not yet been reported. A special misorientation relationship between the texture components of the PCG layer to the orientations of the β-fiber as well as to the B shear component, respectively, are highly probable. Testing the misorientation between the three texture components Brass, S and Copper of the β-fiber against the three texture components of the PCG layer in terms of a rotation around the $\langle 111\rangle$ axis reveals that the S component shows the smallest deviation angle of < 5 deg to the Copper Twin component at 41 deg$\langle 111\rangle$. The misorientation of the Goss and Rotated Cube component to the S component show larger remaining deviation angle of about 14 and 18 deg, respectively, however, these mark the minimum deviation angles to the S component at ~ 40 deg$\langle 111\rangle$. The deviation angle to the $\Sigma 7$ misorientation between the remaining Brass and Copper texture component to the orientations of the PCG layer are much larger. Therefore, preferential growth in terms of $\Sigma 7$ misoriented grain boundaries can only be probable for the growth of the Copper Twin component consuming the S component. Nonetheless, this is the identical relation as in one of the explanations for the dominant Cube recrystallization texture *via* highly mobile grain boundaries that promote grain growth. However, these are only the second-most prominent texture components in their respective microstructural zone. Most grains in the PCG layer are of Rotated Cube orientation, although no favorable misorientation to the dominant Brass component in the bulk can be distinguished. A low-energy $\Sigma 3$ 60 deg$\langle 111\rangle$ twinning relation is existent between Rotated Cube and Copper Twin that might stabilize the selection of both grains, although the high-stacking fault energy in aluminum demotes twinning. The orientation relations found so far can be regarded as first indications on to why favorable growth of grains occurs with distinct $\langle 101\rangle||$TD orientations, however, the prevailing mechanism can only be speculated about so far. Another influence on the kind of PCG formation is probable due to construction of the die orifice. In this study, an identical die was used for all alloys, to keep the deformation conditions and strain state constant. Mahmoodkani *et al.*[39,40] have shown that adjustment to the die orifice design can reduce the formation of PCG due to smaller strain gradients beneath the surface, however,

the shear deformation zone extends deeper into the material.

V. SUMMARY AND CONCLUSION

Five Al–Mg–Si alloys with varying dispersoid content were extruded into a thin-walled extrusion profile at three different extrusion speeds. The microstructure and texture evolution were investigated at a plane section of the extrusion profile by means of EBSD mappings and orientation analysis. From this study the following points can be concluded:

1. It was shown that deformation during extrusion of constant tempered extrusion billets performed at increasing strain rates lead to an increase in profile temperature due to adiabatic heating. The volume fraction and the pinning pressure of dispersoids in Al–Mg–Si extrusion alloys is proportional to the content of dispersoid forming elements (DFE), such as Fe, Mn, Cr, Zr, V and Mo, while the median diameter stays relatively constant. The equilibrium volume fraction of dispersoids and constituent particles was not reached.
2. In case of little grain growth, plane sections of a thin-walled profile lead to a microstructure of elongated grains divided into subgrains with a dominant β-fiber texture, wherein the Brass texture component is dominant. Additionally, a small extent (10− 15 pct) of grains with Cube orientation and spread along the $\langle 001\rangle||$EX-fiber forms.
3. At low-grain boundary mobility, grain growth only occurs in the vicinity of the surface, leading to the formation of the peripheral coarse grain (PCG) layer. Increasing the effective grain boundary mobility with higher extrusion speeds and/or lower dispersoid content leads to the growth of the PCG layer, consuming the fine-grained β-fiber microstructure in the bulk.
4. At medium grain boundary mobility, the extent of the PCG layer is largest, occupying up to 50 pct of the cross-section. However, grain growth in the bulk begins, with growth of grains of Cube components and other orientations of the $\langle 001\rangle||$EX-fiber, that are known as recrystallization texture in Al alloys.
5. At high grain boundary mobility the bulk microstructure is dominated by the formation of grains of Cube and other $\langle 001\rangle||$EX orientations. No β-fiber microstructure is found in the bulk and the PCG extent is decreasing, to the effect that grain growth in the bulk counteracts the formation of a PCG layer.
6. The PCG layer exhibits orientations with a common $\langle 101\rangle||$TD alignment, localized at Rotated Cube, Copper Twin and Goss texture components, with an increasing grain size towards the fine-grained bulk. A proposed mechanism explains the orientation selection in the PCG as promoted by the highly mobile $40\,\mathrm{deg}\langle 111\rangle$ grain boundary misorientation between the Copper Twin component in the PCG and the S component in the bulk.

The findings are expected to be universal to plane sections of a large variety of Al–Mg–Si alloys and profiles. However, the exact deformation conditions depend also on the construction of the extrusion tool and especially the die orifice, which can effect variations in strain state and profile surface temperature.

ACKNOWLEDGMENTS

The study was financially and experimentally supported by the Hammerer Aluminium Industries (HAI) Extrusion GmbH. The authors thankfully acknowledge Anna Hartmann (Friedrich-Alexander-University Erlangen-Nürnberg) for performing the sub-surface target preparation on the samples for EBSD measurement and Marius Kohlhepp (Audi AG Neckarsulm) for assisting with the thermodynamic calculations on JMatPro V10.2.

FUNDING

Open Access funding enabled and organized by Projekt DEAL.

CONFLICT OF INTEREST

The authors declare that they have no known competing financial interests or personal relationships that could have appeared to influence the work reported in this paper.

REFERENCES

1. N. Parson, J. Fourmann, and J.-F. Beland: in *Proc. 11th Alumi. Extrus. Technol. Semin.*, Chicago, 2016, pp. 1–16.
2. Ø. Ryen, B. Holmedal, K. Marthinsen, and T. Furu: *IOP Conf. Ser. Mater. Sci. Eng.*, 2015, vol. 89, 012013.
3. M.S. Remøe, K. Marthinsen, I. Westermann, K. Pedersen, J. Røyset, and C. Marioara: *Mater. Sci. Eng. A*, 2017, vol. 693, pp. 60–72.
4. O. Engler and J. Hirsch: *Mater. Sci. Eng. A*, 2002, vol. 336, pp. 249–62.
5. W.J. Poole, J. Chen, Y. Mahmoodkhani, M.A. Wells, and N.C. Parson: in *Proc. 11th Alumi. Extrus. Technol. Semin.*, Chicago, 2016, pp. 725–34.
6. B.H. Frodal, L. Lodgaard, Y. Langsrud, and T. Børvik: and O.S. Hopperstad *: J. Appl. Mech.*, 2023, vol. 90, 041006.
7. J. Hirsch and K. Lücke: *Acta Metall.*, 1988, vol. 36, pp. 2863–882.
8. J.R. Hirsch: *Mater. Sci. Technol.*, 1990, vol. 6, pp. 1048–57.
9. Jingqi. Chen, W.J. Poole, and N.C. Parson: *Mater. Sci. Eng. A*, 2018, vol. 730, pp. 24–35.
10. O. Daaland and E. Nes: *Acta Mater.*, 1996, vol. 44, pp. 1389–411.
11. O. Daaland and E. Nes: *Acta Mater.*, 1996, vol. 44, pp. 1413–435.
12. J. Grasserbauer, I. Weißensteiner, G. Falkinger, S. Mitsche, P.J. Uggowitzer, and S. Pogatscher: *Materials*, 2020, vol. 13, p. 469.
13. J. Grasserbauer, I. Weißensteiner, G. Falkinger, P.J. Uggowitzer, and S. Pogatscher: *Materials*, 2021, vol. 14, p. 3312.
14. Z. Li, Z. Zhang, G. Zhou, P. Zhao, Z. Jia, and W.J. Poole: *Mater. Sci. Eng. A*, 2021, vol. 814, 141199.
15. G. Falkinger, P. Simon, and S. Mitsche: *Metall. Mater. Trans. A*, 2020, vol. 51, pp. 3066–75.
16. T. Manik, K. Marthinsen, K. Zhang, A.I. Aria, and B. Holmedal: *Front. Mater.*, 2021, vol. 8, 636379.
17. J. Hirsch and K. Lücke: *Acta Metall.*, 1988, vol. 36, pp. 2883–904.
18. B. Sundman, I. Ohnuma, N. Dupin, U.R. Kattner, and S.G. Fries: *Acta Mater.*, 2009, vol. 57, pp. 2896–908.
19. N.C.W. Kuijpers, F.J. Vermolen, C. Vuik, P.T.G. Koenis, K.E. Nilsen, and S. van der Zwaag: *Mater. Sci. Eng. A*, 2005, vol. 394, pp. 9–19.
20. N.C.W. Kuijpers, W.H. Kool, P.T.G. Koenis, K.E. Nilsen, I. Todd, and S. van der Zwaag: *Mater. Charact.*, 2002, vol. 49, pp. 409–20.
21. M. Cooper: *Acta Crystallogr.*, 1967, vol. 23, pp. 1106–107.
22. M. Cooper and K. Robinson: *Acta Crystallogr.*, 1966, vol. 20, pp. 614–17.
23. C.L. Liu, Q. Du, N.C. Parson, and W.J. Poole: *Scr. Mater.*, 2018, vol. 152, pp. 59–63.
24. L. Lodgaard and N. Ryum: *Mater. Sci. Eng. A*, 2000, vol. 283, pp. 144–52.
25. J.A. Österreicher, F. Grabner, A. Schiffl, S. Schwarz, and G.R. Bourret: *Mater. Charact.*, 2018, vol. 138, pp. 145–53.
26. P. Donnadieu, G. Lapasset, and T.H. Sanders: *Philos. Mag. Lett.*, 1994, vol. 70, pp. 319–26.
27. J.D. Robson and P.B. Prangnell: *Acta Mater.*, 2001, vol. 49, pp. 599–613.
28. O. Engler: *Mater. Sci. Technol.*, 1996, vol. 12, pp. 859–72.
29. S. Camero, E.S. Puchi, and G. Gonzalez: *J. Mater. Sci.*, 2006, vol. 41, pp. 7361–373.
30. C. Shi and X.-G. Chen: in *Light Metals*, M. Hyland, ed., Springer International Publishing, Cham, 2015, vol. 2015, pp. 163–67.
31. J. Lai, C. Shi, and X.-G. Chen: *Mater. Charact.*, 2014, vol. 96, pp. 126–34.
32. S. Boczkal, M. Lech-Grega, J. Morgiel, and K. Piela: in *Light Metals*, J. Grandfield, ed., Springer International Publishing, Cham, 2014, vol. 2014, pp. 261–64.
33. A.R. Farkoosh, X. Grant Chen, and M. Pekguleryuz: *Mater. Sci. Eng. A*, 2015, vol. 620, pp. 181–9.
34. W.J. Poole, C. Liu, Z. Zhang, Q. Du, L.R. Pan, and N.C. Parson: in *Proc. 12th Alumi. Extrus. Technol. Semin.*, Orlando, 2022.
35. C.S. Smith: *Trans. Metall. Soc. AIME*, 1948, pp. 15–51.
36. E. Nes, N. Ryum, and O. Hunderi: *Acta Metall.*, 1985, vol. 33, pp. 11–22.
37. Y. Wang, A. Zang, Y. Mahmoodkhani, M. Wells, W. Poole, and N. Parson: *Metall. Mater. Trans. A*, 2021, vol. 52, pp. 3503–516.
38. S. Kaneko, K. Murakami, and T. Sakai: *Mater. Sci. Eng. A*, 2009, vol. 500, pp. 8–15.
39. Y. Mahmoodkhani, M.A. Wells, N.C. Parson, J. Chen, and W.J. Poole: in *Proc. 11th Alumi. Extrus. Technol. Semin.*, Chicago, 2016, pp. 767–79.
40. Y. Mahmoodkhani, J. Chen, M.A. Wells, W.J. Poole, and N.C. Parson: *Metall. Mater. Trans. A*, 2019, vol. 50, pp. 5324–335.
41. M.R. Drury and F.J. Humphreys: *Acta Metall.*, 1986, vol. 34, pp. 2259–271.
42. J.K. Solberg, H.J. McQueen, N. Ryum, and E. Nes: *Philos. Mag. A*, 1989, vol. 60, pp. 447–71.
43. H.J. McQueen, J.K. Solberg, N. Ryum, and E. Nes: *Philos. Mag. A*, 1989, vol. 60, pp. 473–85.
44. M.E. Kassner, H.J. McQueen, and E. Evangelista: *Mater. Sci. Forum*, 1993, vol. 113–115, pp. 151–56.
45. H.J. McQueen and W. Blum: *Mater. Sci. Eng. A*, 2000, vol. 290, pp. 95–107.
46. S. Gourdet and F. Montheillet: *Acta Mater.*, 2002, vol. 50, pp. 2801–812.
47. L. de Pari and W.Z. Misiolek: *Acta Mater.*, 2008, vol. 56, pp. 6174–185.
48. W.H. Van Geertruyden, W.Z. Misiolek, and P.T. Wang: *Mater. Sci. Eng. A*, 2006, vol. 419, pp. 105–14.
49. A. Bandar, W.H. Van Geertruyden, and W.Z. Misiolek: in *Proc. 9th Alumi. Extrus. Technol. Semin.*, Orlando, 2008.
50. A. Güzel, A. Jäger, N. Ben Khalifa, and A.E. Tekkaya: in *Proc. 10th Alumi. Extrus. Technol. Semin.*, Miami, 2012, pp. 603–9.
51. J. Humphreys, G.S. Rohrer, and A. Rollett: in *Recrystallization and Related Annealing Phenomena* , 3rd ed., J. Humphreys, G.S. Rohrer, and A. Rollett, eds., Elsevier, Oxford, 2017.
52. A. Gholinia, F.J. Humphreys, and P.B. Prangnell: *Acta Mater.*, 2002, vol. 50, pp. 4461–476.
53. A. Albou, S. Raveendra, P. Karajagikar, I. Samajdar, C. Maurice, and J.H. Driver: *Scr. Mater.*, 2010, vol. 62, pp. 469–72.
54. H.E. Vatne, T. Furu, and E. Nes: *Mater. Sci. Technol.*, 1996, vol. 12, pp. 201–10.
55. H.E. Vatne and E. Nes: *Scr. Metall. Mater.*, 1994, vol. 30, pp. 309–12.
56. I. Samajdar and R.D. Doherty: *Scr. Metall. Mater.*, 1995, vol. 32, pp. 845–50.
57. W.H. Van Geertruyden, W.Z. Misiolek, and P.T. Wang: in *ASM Int. Conf.*, Pittsburgh, 2003.
58. S.R. Claves, K. Janiszewska, and W.Z. Misiolek: in *Proc. 8th Alumi. Extrus. Technol. Semin.*, Orlando, 2004.
59. W.H. Van Geertruyden, H.M. Browne, W.Z. Misiolek, and P.T. Wang: *Metall. Mater. Trans. A*, 2005, vol. 36, pp. 1049–56.
60. W.H. Van Geertruyden, W.Z. Misiolek, and P.T. Wang: in *Proc. 8th Alumi. Extrus. Technol. Semin.*, Orlando, 2004, pp. 107–14.
61. A.R. Eivani, J. Zhou, and J. Duszczyk: *Philos. Mag.*, 2016, vol. 96, pp. 1188–196.
62. J. Schindelin, I. Arganda-Carreras, E. Frise, V. Kaynig, M. Longair, T. Pietzsch, S. Preibisch, C. Rueden, S. Saalfeld, B. Schmid, J.-Y. Tinevez, D.J. White, V. Hartenstein, K. Eliceiri, P. Tomancak, and A. Cardona: *Nat. Methods*, 2012, vol. 9, pp. 676–82.
63. H. Demers, N. Poirier-Demers, A.R. Couture, D. Joly, M. Guilmain, N. de Jonge, and D. Drouin: *Scanning*, 2011, vol. 33, pp. 135–46.
64. F. Bachmann, R. Hielscher, and H. Schaeben: *Solid State Phenom.*, 2010, vol. 160, pp. 63–68.
65. F. Montheillet, M. Cohen, and J.J. Jonas: *Acta Metall.*, 1984, vol. 32, pp. 2077–89.
66. C.l. Maurice and JH Driver: *Acta Mater.*, 1997, vol. 45, pp. 4627–638.
67. C.l. Maurice and J.H. Driver: *Acta Mater.*, 1997, vol. 45, pp. 4639–649.
68. F. Perocheau, and J.H. Driver: *Int. J. Plast.*, 2002, vol. 18, pp. 185–202.
69. O. Engler: *Acta Mater.*, 1998, vol. 46, pp. 1555–568.
70. D.A. Molodov, L.S. Shvindlerman, and G. Gottstein: *Int. J. Mater. Res.*, 2003, vol. 94, pp. 1117–126.